ANALYSIS OF UNSTEADY FLOWS AROUND WING PROFILES AT LONGITUDINAL ACCELERATIONS

ICAS-94-2.8.1

Ilham A. Habibie, Boris Laschka, Caroline Weishäupl
Scientific Assistant, Full Professor of Fluid Mechanics, Scientific Assistant
Lehrstuhl für Fluidmechanik, Technische Universität München,
D-80290 München,
Germany

Abstract

The present paper is concerned with unsteady flows around airfoils and, in particular, with longitudinal accelerations and decelerations. Solutions are achieved by using the basic Euler equations in an accelerated coordinate system. After a general classification of unsteady flows the specific features associated with unsteady longitudinal flows are addressed. The Euler equations in its standard flux formulation given in an inertial system will be extended to a body–fixed (accelerated) coordinate system by applying a Galilei transformation in all three spatial directions. With regard to these special equations an Euler code is developed. Results for a horizontally accelerated and oscillating NACA 0012 airfoil are studied thoroughly. Special emphasis is laid here on the formation and the decay of shocks and the acceleration through the sonic region. It is found that the inertia of the shock motion has big influence on the time lag of the aerodynamic forces.

Nomenclature

Symbols

α	angle of attack
κ	ratio of specific heats
λ	eigenvalue
$\overline{\Phi}$	vector of conservative flow variables
ρ	density
τ	reduced time
ξ, η, ζ	curvilinear coordinates
a	acceleration
$\underline{A}$	Jacobian matrix in ξ–direction
c	speed of sound
c	wing chord
e	total energy per unit volume
$\overline{E}, \overline{F}, \overline{G}$	fluxes in ξ, η, ζ–direction
Fr	Froude number
g	constant of gravity
H	total enthalpy
$H(\tau)$	Heaviside function
J	Jacobian of coordinate transformation
k	reduced frequency
l	characteristic length
$\underline{L}$	matrix of left eigenvectors
M	Mach number
p	static pressure
q	dynamic pressure
$\underline{R}$	matrix of the right eigenvectors
t	time
T	ramp time
u, v, w	velocities in x, y, z–direction
U, V, W	contravariant velocities in ξ, η, ζ–direction
$\overline{V}$	velocity vector
x, y, z	cartesian coordinates
$\dot{x}, \dot{y}, \dot{z}$	grid node velocities in x, y, z–direction

Subscripts

crit	critical
d	drag
k	body–fixed coordinate system
l	lift
m	moment
m	momentary
p	static pressure
0	initial value
∞	undisturbed flow

Introduction

Unsteady flows occuring at an aircraft configuration influence significantly the dynamics of the aircraft and its components. Consequently, they play an important role, in particular, to ensure the safety of the airplane.

In general, unsteady flows may be referred to rotational and translational motions. The latter one can be further subdivided in longitudinally, laterally, vertically accelerated ones, Fig. 1. Arbitrary accelerated flows are obtained by superposition of the unidirectional components. Furtheron all these flow types can be created in an active or passive manner, namely by an unsteady motion of the considered body itself or by the unsteady flowfield affecting this body.

Relevant investigations on this subject mainly deal with vertical accelerated unsteady flows, especially, those induced by pitching and heaving oscillations of an airfoil, corresponding to a variation of angle of attack. Although longitudinally accelerated flows, corresponding to Mach number variations, are in comparison to the latter flow type less investigated, they may be of great importance, as shown by experimental results, Fig. 2: The effect of Mach number and angle of attack variation on shock strength and position in the transonic velocity regime substantiate that already small Mach number variations have a considerable influence.

The complex flow physics going along with longitudinally accelerated flows is illustrated by the wave propagation of a source accelerated from subsonic to supersonic region, Fig. 3.[1] It is well–known that at uniform velocities any field point is affected by one disturbance at subsonic conditions and by two at supersonic ones. For uniformly accelerated flows up to four disturbances emitted at different times may reach one field point simultaneously.

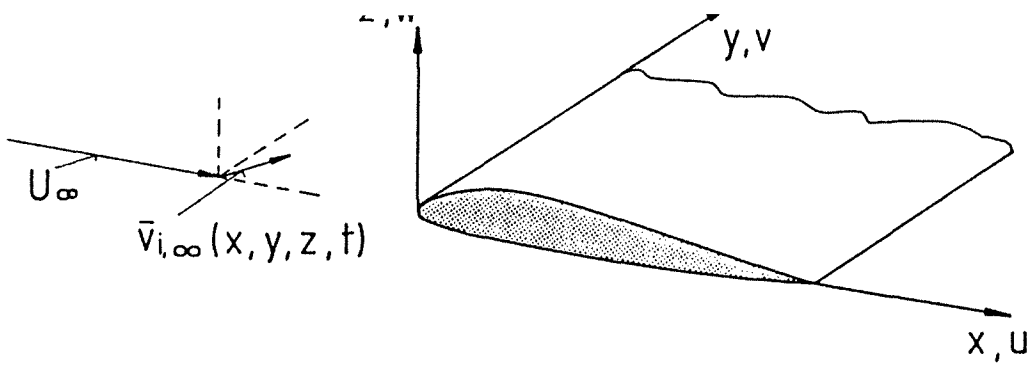

Fig. 1 Superposition of unsteady velocity vectors.

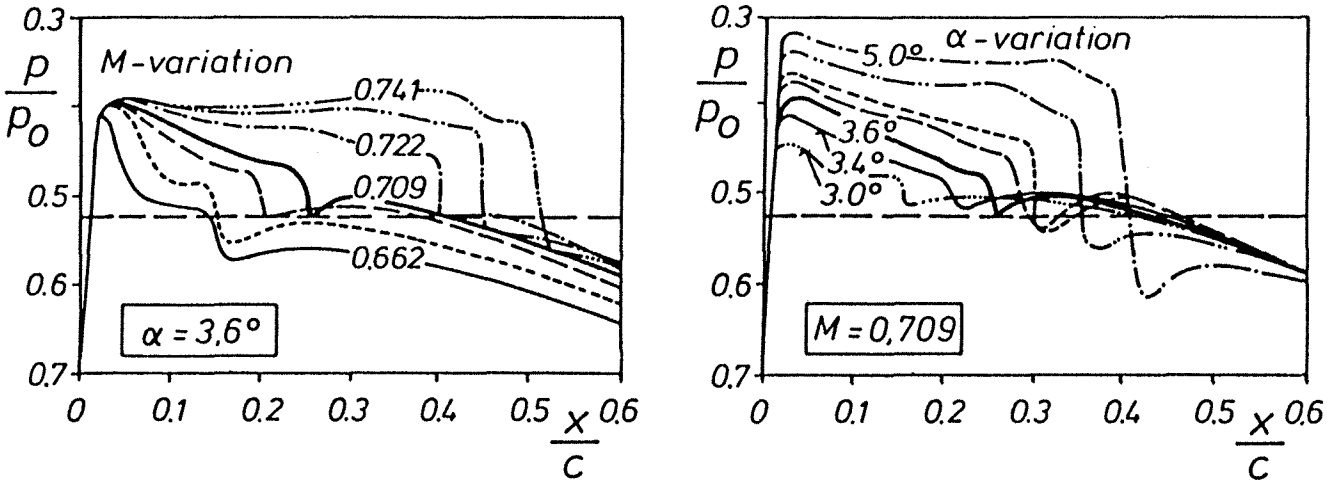

Fig. 2 Sensitivity of upper side wing pressures with respect to Mach number and angle of attack variations.[1]

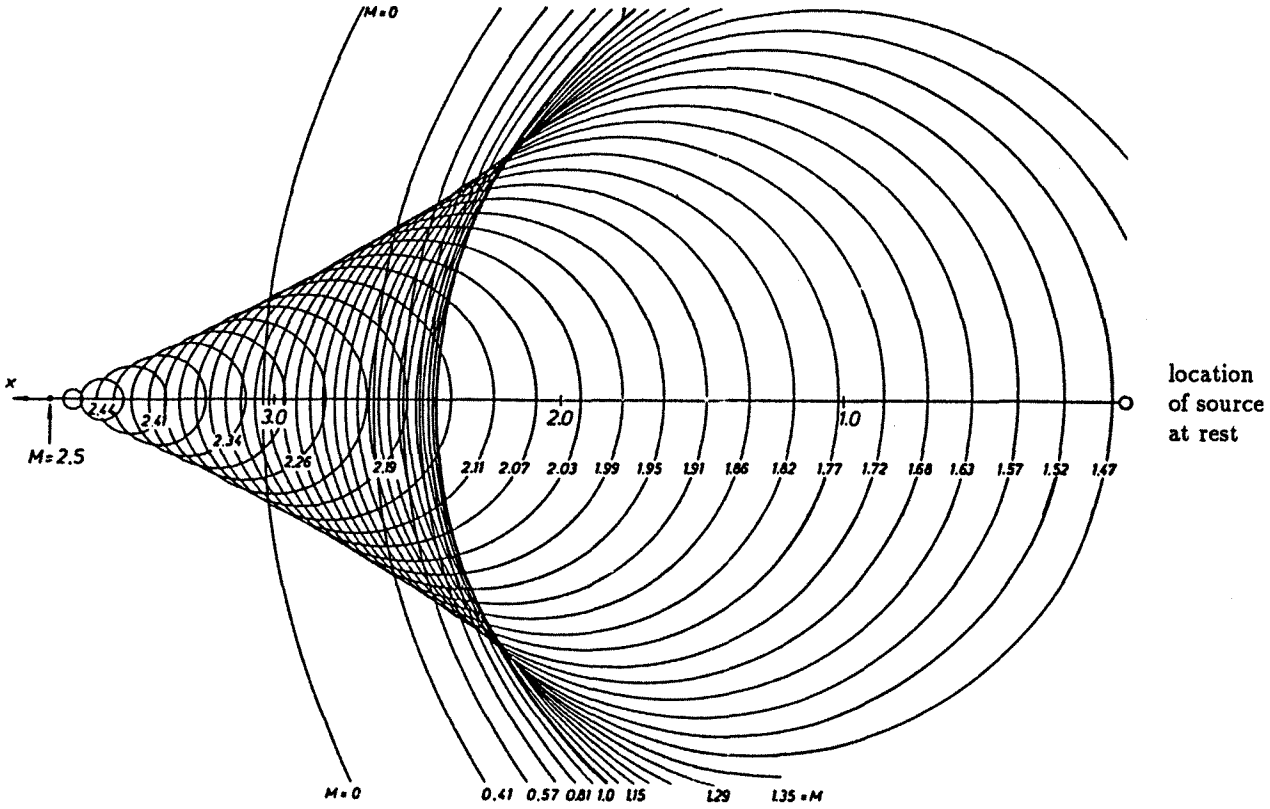

Fig. 3 Wave pictures for a source starting from rest and accelerating to Mach number 2.5, with $\partial M/\partial \tau = c/\sqrt{a\,l} = 1.1$.[1]

Longitudinally accelerated flows occur in following practical cases. An incoming unsteady flowfield can be caused e.g. by horizontal gusts, shear winds and microbursts, which occur in thunderstorms. This atmospheric phenomenon is responsible for several serious flight accidents [2] and, therefore, detailed investigations are needed. On the other hand, longitudinal unsteady motions of the body itself result in Mach number changes, like discontinuities, ramps, oscillations etc. of an airfoil. Such Mach number changes occur at specific oscillations of aircraft components, e.g. a T-tail, yawing motions, in-plane oscillations at variable-swept-wing configurations and at rotor blades, for the latter whenever the free flow is not aligned with the rotor axis.

In order to analyze flowfields corresponding to longitudinally accelerated flows by a numerical method the basic equations can be formulated in two different reference systems:

(a) An inertial aerodynamic coordinate system or
(b) a coordinate system fixed to the considered longitudinally accelerated body.

The inertial one is characterized by following features: A mesh, used for the discretization of the evaluation regime, is to be adapted to the new position of the body at each time step. Either, this requires a great effort with grid generation causing much higher CPU-time or it results in a loss of mesh quality. Furtheron, in order to calculate the flow around a body longitudinally moved relative to the coordinate system for a longer time period, a large logitudinal grid extension is required. In addition, the CPU-time is increased when using boundary conditions at the body which have to consider the relative motion of the body to the mesh.

Against the inertial system a coordinate system accelerated with the body enables the use of a mesh which remains unchanged during the computing time. This means that a high mesh quality can be guaranteed over the whole time. Also long-range body motions in longitudinal direction do not require a corresponding enlargement of the mesh. Furtheron, less effort is needed to formulate the boundary conditions at the body because there is no motion of the body relative to the mesh.

Comparing the features of the two described reference systems, one can easily see, for the calculation of flowfields around longitudinally accelerated bodies a system fixed to the body is the preferable one.

In this paper the cases of steep Mach number ramps and Mach number oscillations are selected from the large field of longitudinally accelerated flows. They are of major interest in the transonic and supersonic regime because here already small changes in Mach number lead to significant changes in aerodynamic loads. E.g. Mach number changes of 1% correspond with accelerations to some 10 g.[3]

The performed calculations deal with unsteady, inviscid flow around a NACA 0012 airfoil using a finite-volume Euler method. As above revealed a body-fixed reference system is especially suited for the numerical analysis.

Fundamentals

The analytical basis are the conservative Euler equations in differential form. These equations are formulated subsequently in curvilinear coordinates using a reference system fixed in space.[4]

$$\frac{\partial \overline{\Phi}}{\partial \tau} + \frac{\partial \overline{E}}{\partial \xi} + \frac{\partial \overline{F}}{\partial \eta} + \frac{\partial \overline{G}}{\partial \zeta} = 0 \tag{1}$$

$\overline{\Phi}$ is the vector of the conservative flow variables, $\overline{E}$, $\overline{F}$, $\overline{G}$ are the fluxes in the curvilinear coordinates ξ, η, ζ.

$$\overline{\Phi} = J \begin{pmatrix} \rho \\ \rho u \\ \rho v \\ \rho w \\ e \end{pmatrix} \qquad \overline{E} = J \begin{pmatrix} U \\ U\,u + p\,\xi_x \\ U\,v + p\,\xi_y \\ U\,w + p\,\xi_z \\ U\,H \end{pmatrix}$$

$$\overline{F} = J \begin{pmatrix} V \\ V\,u + p\,\eta_x \\ V\,v + p\,\eta_y \\ V\,w + p\,\eta_z \\ V\,H \end{pmatrix} \qquad \overline{G} = J \begin{pmatrix} W \\ W\,u + p\,\zeta_x \\ W\,v + p\,\zeta_y \\ W\,w + p\,\zeta_z \\ W\,H \end{pmatrix}$$

Herein H stands for the total enthalpy

$$H = \frac{\kappa e}{\rho} - \frac{\kappa - 1}{2\,\rho^2}\left((\rho u)^2 + (\rho v)^2 + (\rho w)^2\right)$$

and U, V, W denote the contravariant velocities in ξ, η, ζ-direction.

$$\begin{aligned} U &= \rho\,(u - \dot{x})\,\xi_x + \rho\,(v - \dot{y})\,\xi_y + \rho\,(w - \dot{z})\,\xi_z \\ V &= \rho\,(u - \dot{x})\,\eta_x + \rho\,(v - \dot{y})\,\eta_y + \rho\,(w - \dot{z})\,\eta_z \\ W &= \rho\,(u - \dot{x})\,\zeta_x + \rho\,(v - \dot{y})\,\zeta_y + \rho\,(w - \dot{z})\,\zeta_z \end{aligned}$$

Galilei-transformed Euler Equations

Galilei Transformation

The Galilei transformation is used to transform a function from a coordinate system fixed in space characterized by x, y, z, t into a translationally moved system x_k, y_k, z_k, $t_k = t$.

The transformal function requires the knowledge of the relative velocity $\overline{V}_0 = (U_0, V_0, W_0)$ between the two regarded systems. In particular, arbitrary time-dependent functions of velocity $\overline{V}_0(t)$ are possible.

Hence, the transformal function can be written as

$$\begin{pmatrix} x \\ y \\ z \\ t \end{pmatrix} = \begin{pmatrix} x_k - \int_0^t U_0\,(t')\,d\,t' \\ y_k - \int_0^t V_0\,(t')\,d\,t' \\ z_k - \int_0^t W_0\,(t')\,d\,t' \\ t_k \end{pmatrix} \tag{2}$$

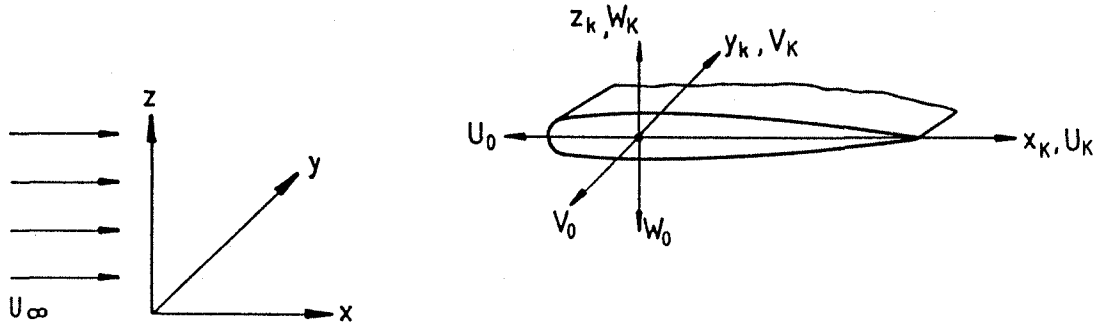

Fig. 4 Galilei transformation,[3]
U_∞ free stream velocity,
(U_k, V_k, W_k) body velocity relative to coordinate system x, y, z,
$(U_0, V_0, W_0) = -(U_k, V_k, W_k)$ flow velocity increment to body motion.

In order to apply the Galilei transformation to the analysis of flows around translationally moved bodies the velocity vector of the body $\overline{V}_k(t)$ is to be used as $-\overline{V}_0(t)$, see Fig. 4.

To obtain the velocity $\overline{v}_k$ in the body-fixed system $\overline{V}_0$ is added to the velocity $\overline{v}$ in the system fixed in space.

$$\overline{v}_k = \overline{v} + \overline{V}_0 \tag{3}$$

Written in nondimensional, curvilinear coordinates [3] the transformation provides the following relationship for the derivatives between the two systems:

$$\begin{pmatrix} \frac{\partial}{\partial \xi} \\ \frac{\partial}{\partial \eta} \\ \frac{\partial}{\partial \zeta} \\ \frac{\partial}{\partial \tau} \end{pmatrix} = \begin{pmatrix} \frac{\partial}{\partial \xi_k} \\ \frac{\partial}{\partial \eta_k} \\ \frac{\partial}{\partial \zeta_k} \\ U_0(\tau)\frac{\partial}{\partial \xi_k} + V_0(\tau)\frac{\partial}{\partial \eta_k} + \\ + W_0(\tau)\frac{\partial}{\partial \zeta_k} + \frac{\partial}{\partial \tau_k} \end{pmatrix} \tag{4}$$

Euler Equations In A Body-fixed Coordinate System

Applying Eq. (4) to Eq. (1), the Galilei-transformed Euler equations

$$\frac{\partial \overline{\Phi}_k}{\partial \tau_k} + \frac{\partial \overline{E}_k}{\partial \xi_k} + \frac{\partial \overline{F}_k}{\partial \eta_k} + \frac{\partial \overline{G}_k}{\partial \zeta_k} = 0 \tag{5}$$

with

$$\overline{\Phi}_k = J \begin{pmatrix} \rho_k \\ \rho_k (u_k - U_0) \\ \rho_k (v_k - V_0) \\ \rho_k (w_k - W_0) \\ e_k - e_0 \end{pmatrix}$$

$$\overline{E}_k = J \begin{pmatrix} U_k \\ U_k (u_k - U_0) + p_k \xi_{k,x} \\ U_k (v_k - V_0) + p_k \xi_{k,y} \\ U_k (w_k - W_0) + p_k \xi_{k,z} \\ \frac{U_k}{\rho}(e_k - e_0) + \frac{U_{0,k}}{\rho} p_k \end{pmatrix}$$

$$\overline{F}_k = J \begin{pmatrix} V_k \\ V_k (u_k - U_0) + p_k \eta_{k,x} \\ V_k (v_k - V_0) + p_k \eta_{k,y} \\ V_k (w_k - W_0) + p_k \eta_{k,z} \\ \frac{V_k}{\rho}(e_k - e_0) + \frac{V_{0,k}}{\rho} p_k \end{pmatrix}$$

$$\overline{G}_k = J \begin{pmatrix} W_k \\ W_k (u_k - U_0) + p_k \zeta_{k,x} \\ W_k (v_k - V_0) + p_k \zeta_{k,y} \\ W_k (w_k - W_0) + p_k \zeta_{k,z} \\ \frac{W_k}{\rho}(e_k - e_0) + \frac{W_{0,k}}{\rho} p_k \end{pmatrix}$$

are obtained.

The contravariant velocities $\overline{V}_k$ and $\overline{V}_{0,k}$ are defined as follows

$$\begin{aligned} U_k &= \rho_k u_k \xi_{k,x} + \rho_k v_k \xi_{k,y} + \rho_k w_k \xi_{k,z} \\ V_k &= \rho_k u_k \eta_{k,x} + \rho_k v_k \eta_{k,y} + \rho_k w_k \eta_{k,z} \\ W_k &= \rho_k u_k \zeta_{k,x} + \rho_k v_k \zeta_{k,y} + \rho_k w_k \zeta_{k,z} \end{aligned}$$

and

$$
\begin{aligned}
U_{0,k} &= \rho_k (u_k - U_0)\,\xi_{k,x} + \rho_k (v_k - V_0)\,\xi_{k,y} + \\
&\quad \rho_k (w_k - W_0)\,\xi_{k,z} \\
V_{0,k} &= \rho_k (u_k - U_0)\,\eta_{k,x} + \rho_k (v_k - V_0)\,\eta_{k,y} + \\
&\quad \rho_k (w_k - W_0)\,\eta_{k,z} \\
W_{0,k} &= \rho_k (u_k - U_0)\,\zeta_{k,x} + \rho_k (v_k - V_0)\,\zeta_{k,y} + \\
&\quad \rho_k (w_k - W_0)\,\zeta_{k,z}
\end{aligned}
$$

The speed of sound and the density are invariant towards the transformation and consequently also the pressure remains unchanged.

$$
\begin{aligned}
\rho_k &= \rho \\
p_k &= p
\end{aligned}
$$

Corresponding to Eq. (3) the total energy per unit volume is given by

$$
\begin{aligned}
e_k &= e + e_0 = \frac{p}{(\kappa - 1)} + \frac{\rho}{2}\,(u^2 + v^2 + w^2) + \\
&\quad \rho\,(u\,U_0 + v\,V_0 + w\,W_0) + \frac{\rho}{2}\,(U_0^2 + V_0^2 + W_0^2)
\end{aligned}
$$

Euler-code

The here applied Euler-code, named GEOFLEX, is an improvement of the well-known code EUFLEX, an Euler code with characteristic flux extrapolation.[5] Compared to EUFLEX, GEOFLEX provides an adequate physical treatment of an expansion wave by an entropy-correction based on the geometry of the expansion wave in a path-time diagram.[6] In addition, the described Galilei transformation from an inertial to an accelerated body-fixed system is implemented.

To solve the basic equations Eq. (5) in the body-fixed system, GEOFLEX employs dimension-splitting leading to

$$
\left(\frac{\partial \overline{\Phi}_k}{\partial \tau_k}\right)_{\xi_k} + \frac{\partial \overline{E}_k}{\partial \xi_k} = 0
$$

e.g. in ξ_k-direction. Introducing a corresponding Jacobian

$$
\underline{A}_k = \frac{\partial \overline{E}_k}{\partial \overline{\Phi}_k}
$$

the equation can be written as

$$
\left(\frac{\partial \overline{\Phi}_k}{\partial \tau_k}\right)_{\xi_k} + \underline{A}_k \frac{\partial \overline{\Phi}_k}{\partial \xi_k} = 0
$$

Analogous formulations are obtained for the η_k- and ζ_k-direction. The evaluation of the flow variables at the cell border, i.e. the solution of the Riemann problem, needs the determination of the eigenvalues $\lambda_{i\,k}$ and corresponding left and right eigenvectors $L_{i\,k}$ and $R_{i\,k}$ of the Jacobian. The eigenvalues are

$$
\lambda_{0,1,2\,k} = u_k, \qquad \lambda_{3\,k} = u_k + c, \qquad \lambda_{4\,k} = u_k - c
$$

The matrices of the eigenvectors $\underline{L}_k$ and $\underline{R}_k$ are given in the appendix. Thus, the flow variables $\overline{\Phi}_k$ at the cell border can be calculated.[7] A flux balance over the cell results in the flow variables at the new time step.

GEOFLEX uses a second order discretization in space and first order in time. Wiggles at shock fronts are avoided by a limiter switching from second order back to first order in space. The time characteristics of unsteady flows lead to a limitation of the possible time step and, therefore, an explicit scheme is appropriate.

Characteristic [8] and absorbing [9] farfield boundary conditions are implemented and, therefore, the distance between the farfield bound and the body can be significantly reduced. Correct flow conditions at the body are achieved by characteristic and kinematic [10] boundary conditions.

The discretization of the calculation regime corresponding to the considered two dimensional flows is realized by an elliptic H-type grid with 72 × 48 grid points.[3,10]

Results And Discussion

Validation

First, to validate the modified Euler code formulated in the body-fixed coordinate system, for a NACA 0012 airfoil obtained results are compared with the results of GEOFLEX and two other Euler codes,[11,12] formulated in an inertial system. The presented results refer to a relative simple testcase, namely a steep Mach number ramp given by

$$
M(\tau) = M_0 + \Delta M\,\frac{\tau}{T} \qquad 0 < \tau < T \tag{6}
$$

with $M_0 = 0$, $\Delta M = 0.8$, $\alpha = 2°$ and $\tau \to 0$.

Fig. 5a shows the development of the lift coefficient over the time, the corresponding moment coefficient is presented in Fig. 5b: The results of the four codes agree very well, although different meshes were used.

Secondly, the validity of the Euler code in the body-fixed coordinate system for unsteady flows is to be substantiated by a testcase, which is evaluated with both, the new body-fixed method and the corresponding well-known inertial one. Here a horizontal oscillation described by

$$
M(\tau) = M_0 + M_1 \cos(k\tau) \tag{7}
$$

with $M_0 = 0.738$, $M_1 = 0.062$, $k = 0.8$ and $\alpha = 2°$ is chosen. To compare the results of the two methods, the Lissajous figures of the lift coefficient, Fig. 6a, and of the drag coefficient, Fig. 6b, over the time-dependent Mach number of incoming flow are analyzed. A good agreement between the two methods is evident, the occuring deviation can be explained by the variable mesh quality using the inertial code.

The two considered cases show that GEOFLEX, formulated in the body-fixed coordinate system, is able to calculate unsteady longitudinally accelerated flows correctly.

Analysis

To analyze the accelerated, unsteady flow the code in the body-fixed coordinate system is applied to two types of motions of the NACA 0012 profile

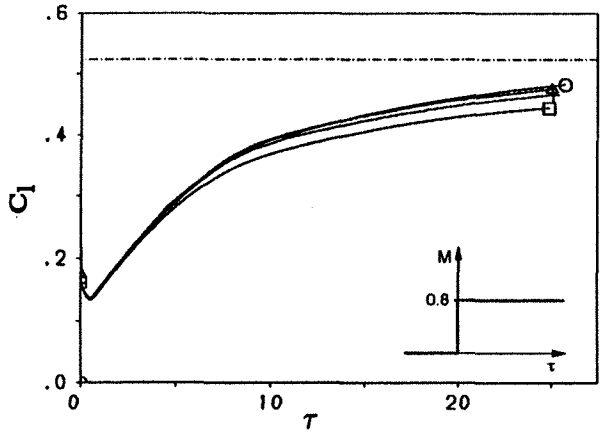

Fig. 5a Lift coefficient for a steep Mach number ramp,
$M_0 = 0$, $\Delta M = 0.8$, $\alpha = 2°$, $\tau \to 0$,
o Euler code in inertial formulation,[12]
△ GEOFLEX in body-fixed formulation,
+ GEOFLEX in inertial formulation,
□ Euler code in inertial formulation,[11]
– · – steady.

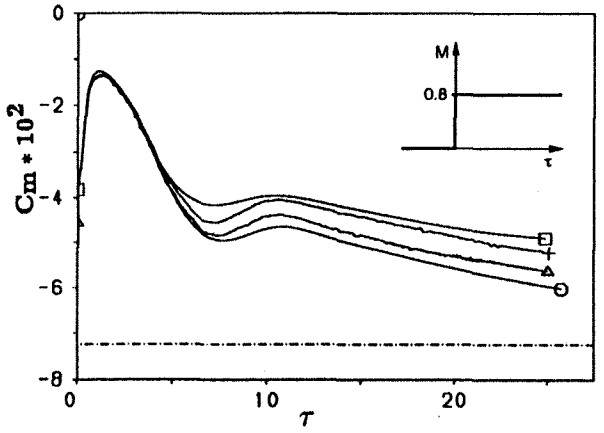

Fig. 5b Moment coefficient for a steep Mach number ramp,
$M_0 = 0$, $\Delta M = 0.8$, $\alpha = 2°$, $\tau \to 0$,
o Euler code in inertial formulation,[12]
△ GEOFLEX in body-fixed formulation,
+ GEOFLEX in inertial formulation,
□ Euler code in inertial formulation,[11]
– · – steady.

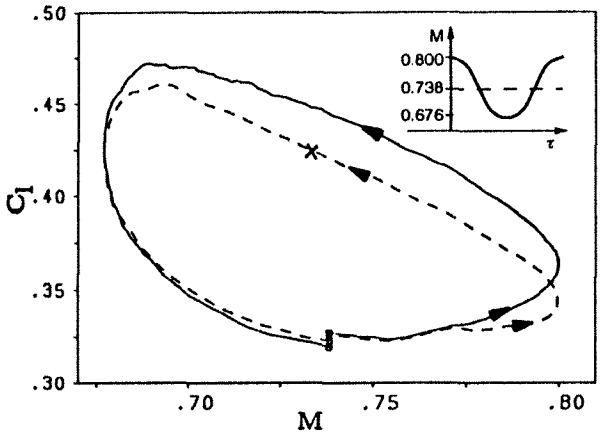

Fig. 6a Lift coefficient for horizontal oscillations,
$M_0 = 0.738$, $M_1 = 0.062$, $\alpha = 2°$, $k = 0.8$,
□ GEOFLEX in body-fixed formulation,
× GEOFLEX in inertial formulation.

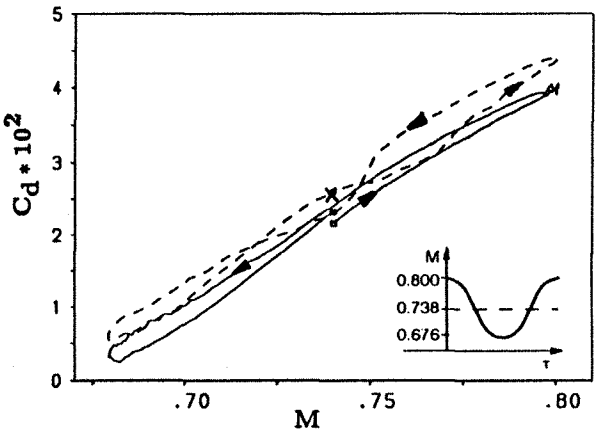

Fig. 6b Drag coefficient for horizontal oscillations,
$M_0 = 0.738$, $M_1 = 0.062$, $\alpha = 2°$, $k = 0.8$,
□ GEOFLEX in body-fixed formulation,
× GEOFLEX in inertial formulation.

- Acceleration from subsonic to transonic Mach number
- Horizontal (in-plane) oscillations

Acceleration From Subsonic To Transonic Mach Number

Starting from a low subsonic Mach number $M = 0.4$ the airfoil accelerates to a transonic Mach number $M = 0.8$. The angle of attack is $\alpha = 2°$.
The Mach number function is given by

$$M(\tau) = M_0 + \Delta M \frac{\tau}{T} \qquad 0 < \tau < T \tag{8}$$

with $M_0 = 0.4$ and $\Delta M = 0.4$, the acceleration is constant, it is finished after $T = 5$.
It was of special interest here to look at the generation of the shock.
Fig. 7 shows the time history for the pressure distributions.

After $\tau = 0.1$ the local disturbance has propagated from the trailing edge to $x/c = 0.9$ shown by the two kinks. At $\tau = 10$ two shocks are visible, a strong shock on the upper side and a weak shock on the lower side of the airfoil. Whereas with increasing time the shock on the upper side gains in strength the shock on the lower side decays and vanishes.

The lift coefficient, see Fig. 8, reaches the steady state value asymptotically. As is also known from the initial lift behaviour of sudden incidence changes after the beginning a drop in the lift coefficient is observed before the lift recovers.

Horizontal Oscillations At Small Amplitudes

Horizontal oscillations are of major interest at flutter calculations where in-plane motions of the airfoil - occuring

e.g. at airplanes with variable sweep - play an important role. If the flow is transonic, periodic shock motions go along with the oscillations. Aerodynamic coefficients are largely affected. The Mach number function taken is

$$M(\tau) = M_0 + H(\tau)\,\Delta M\,\cos(k\,\tau) \qquad (9)$$

The airfoil is investigated at an incidence of $\alpha = 2°$. The Mach number $M_0 = 0.8$ and the amplitude $\Delta M = 0.01$ are such that complex transonic flow conditions occur. A low and a high reduced frequency ($k = 0.1$ and $k = 0.5$) are chosen.

Fig. 9 compares the lift coefficient c_l as function of the Mach number for the steady and the unsteady case at $k = 0.5$. The unsteady lift has a phase shift compared to the steady case as expected in unsteady motions. This is mainly caused by the difference between the position of the shock at steady and unsteady conditions, as is recognized from the pressure distribution, see Fig. 10.

The time lag for the lift coefficient increases with increasing reduced frequency k, see Fig. 9 and Fig. 11.

Horizontal Oscillations Leading To Shock Formation And Decay

Steady calculations for the NACA 0012 airfoil reveal that at a Mach number of $M = 0.738$ and at a zero angle of attack the flow is highly subsonic but still shockfree. When the Mach number increases strong shocks develop around the airfoil. Hence, a motion of the airfoil which starts at $M = 0.738$ and accelerates sinusoidally up to $M = 0.8$ and finally decelerates down to $M = 0.676$ is investigated.

This case was initially studied by Grünspahn, who used an Euler code based on a bicharacteristic method.[13] The data presented in his work are documented in a way that does not permit more than a qualitative comparison. Also, the shock resolution there is of minor quality due to wiggles.

The Mach number function is given graphically by Grünspahn and is approximated by

$$M(t) = \begin{cases} M_{0,1} + \Delta M_1\,\cos(\omega\,(t - t_0)), & t < t_0 \\ M_{0,2} + \Delta M_2\,\cos(\omega\,(t - t_0)), & t > t_0 \end{cases} \qquad (10)$$

with $\omega = 196.4\,[1/s]$ and $t_0 = 0.016\,[s]$, $M_{0,1} = 0.769$, $M_{0,2} = 0.738$, $\Delta M_1 = 0.031$ and $\Delta M_2 = 0.062$. Here, unusually the Mach number is a function of real time.

The pressure distributions for GEOFLEX compared to the results given in Ref. 13, see Fig. 12, show that GEOFLEX produces wiggle–free pressure distributions, which is not the case for the Grünspahn code. This is due to the fact that GEOFLEX, as a finite volume code, uses a limiter to overcome numerical oscillations at shocks. It is assumed that the code of Grünspahn does not possess enough numerical dissipation to produce the same quality of shock-representation.

As depicted in Fig. 13b,c the two codes show generally similar behaviour of the drag coefficient versus time, corresponding to the regarded Mach number function, Fig. 13a. Grünspahn[13] chooses as reference value of the drag coefficient $c_d = 0$ for the initial Mach number $M_0 = 0.738$. This is not taken for the present case. Instead, here a slightly positive drag value resulting from GEOFLEX is chosen as reference drag value. Differences may be referred to a smaller immanent numerical dissipation of the Grünspahn code in comparison to GEOFLEX. Furtheron, Grünspahn uses much more grid points to discretize the evaluation regime, this leads also to a decrease in drag.

For both methods the maximum values of the drag coefficient occur approximately at the same time. Negative values are revealed always in connection with a shock movement towards the leading edge, as can be seen from the isobares at $t = 0.063\,[s]$, see Fig. 14.

The comparison of the unsteady pressure coefficient distribution at the airfoil with the steady values shows the large time lag of the shock position, see Fig. 15. The difference between the two is larger than for oscillations at small amplitudes.

In order to better understand the influence of the shock strength, the same Mach number function was taken for an angle of attack of $\alpha = 2°$. The corresponding pressure distribution is presented in Fig. 16, the lift coefficient in Fig. 17. Regarding the pressure distribution at the airfoil it is obvious that the time lag effect is dominated by the upper side and this results in a time lag for the lift coefficient also.

Horizontal Oscillations Around The Speed Of Sound

The transition through the sonic region has always attracted the interest. But no investigation known has taken the effect of acceleration into consideration. Due to this calculations are made where the airfoil is decelerated from a supersonic Mach number to a subsonic and, in return accelerated to the initial Mach number. The Mach number function here is similar to that for the oscillations with small amplitudes, see Eq. (9), with $M_0 = 1.0$ and $\Delta M = 0.05$. The reduced frequency is $k = 0.5$ and the angle of attack $\alpha = 2°$.

The frequency chosen is not of practical importance but the main purpose of this example is to demonstrate the capability of GEOFLEX. A lower frequency would have resulted in much higher computing time.

If we compare the steady with the unsteady pressure coefficient distribution around the airfoil, see Fig. 18, it is quite obvious that unsteadiness has a smaller influence than in the velocity regime around $M = 0.738$ to 0.8 which has been discussed before. This is because in the sonic region the shock remains in the trailing edge. There its influence on the flow at the profile is small. This can also be noticed in the unsteady lift coefficient, see Fig. 19. Compared to the quasisteady lift the unsteadiness results in a higher amplitude but only in a small phase shift.

Conclusions

A numerical method especially suited to the solution of flows around unsteady longitudinally accelerated airfoils has been presented. The starting point is the formulation of the conservative Euler equations in differential form using curvilinear coordinates. In particular, for the longitudinal

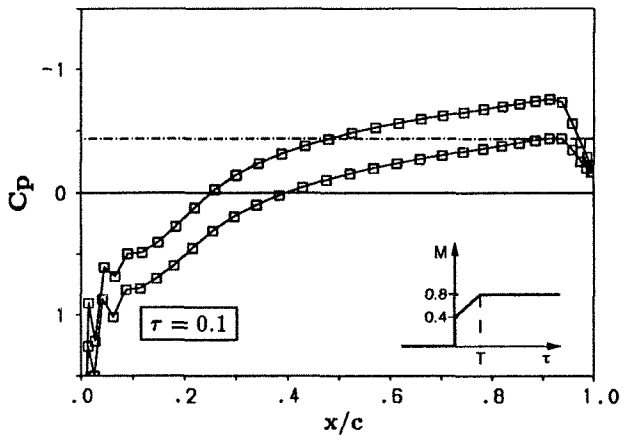

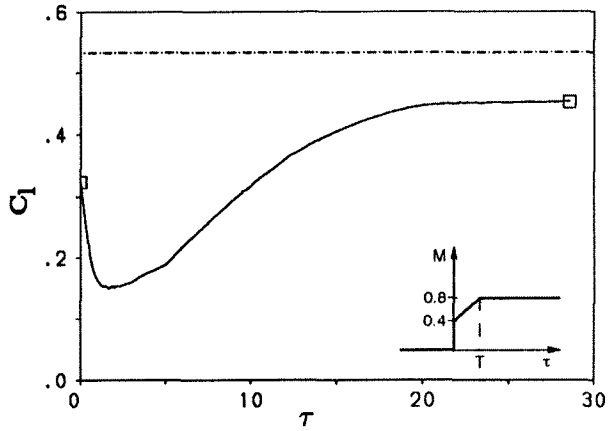

Fig. 8 Lift coefficient for horizontal acceleration from subsonic to transonic Mach number,
$M = 0.4 \rightarrow 0.8$, $\alpha = 2°$, $T = 5$,
□ unsteady, — · — steady.

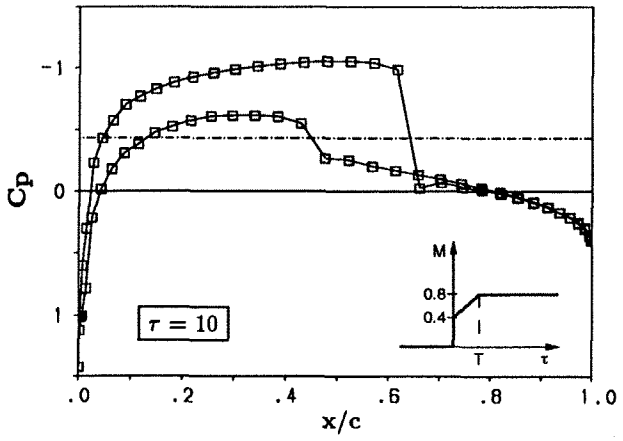

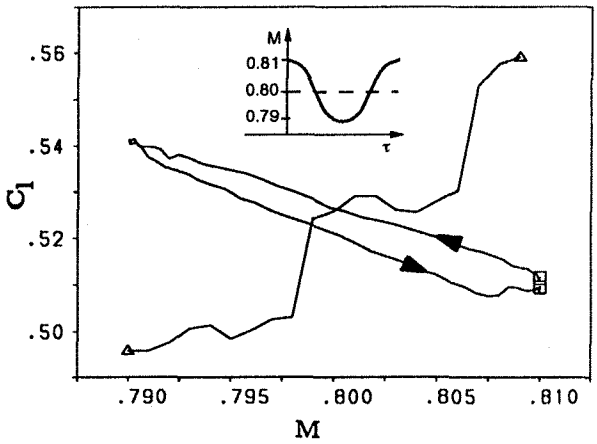

Fig. 9 Lift coefficient for horizontal oscillations at small amplitudes,
$M_0 = 0.8$, $\Delta M = 0.01$, $\alpha = 2°$, $k = 0.5$,
□ unsteady, △ steady.

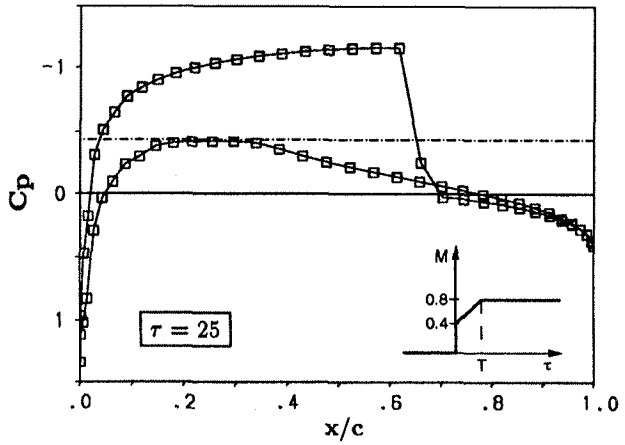

Fig. 7 Pressure distribution for horizontal acceleration from subsonic to transonic Mach number,
$M = 0.4 \rightarrow 0.8$, $\alpha = 2°$, $T = 5$,
$- \cdot - c_{p_{crit}}$.

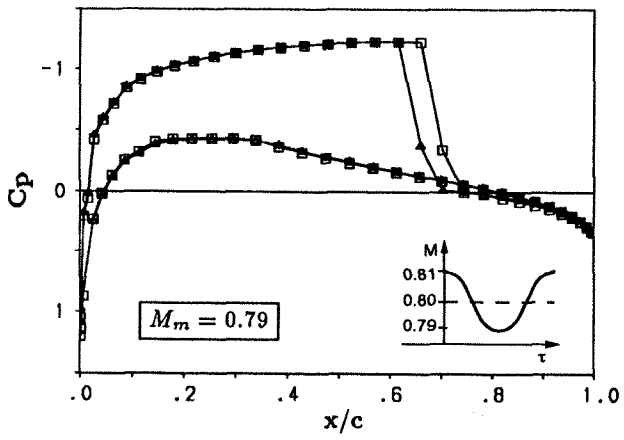

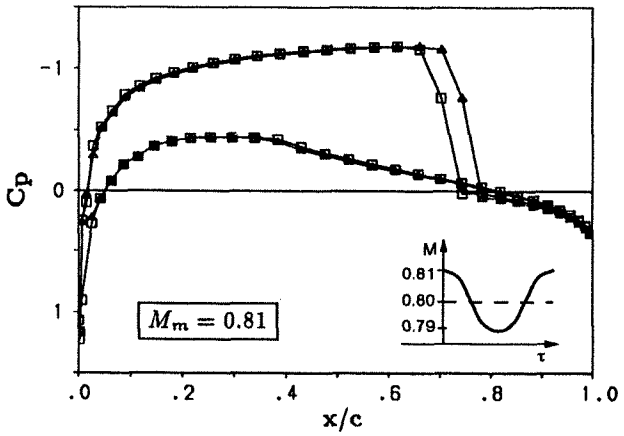

Fig. 10 Pressure distribution for horizontal oscillations at small amplitudes,
$M_0 = 0.8$, $\Delta M = 0.01$, $\alpha = 2°$, $k = 0.5$,
□ unsteady, △ steady.

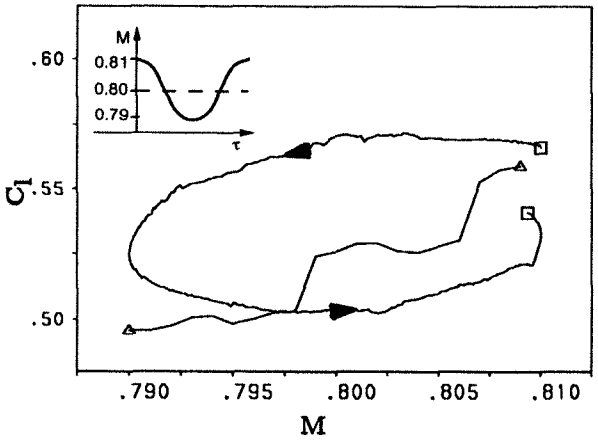

Fig. 11 Lift coefficient for horizontal oscillations at small amplitudes,
$M_0 = 0.8$, $\Delta M = 0.01$, $\alpha = 2°$, $k = 0.1$,
□ unsteady, △ steady.

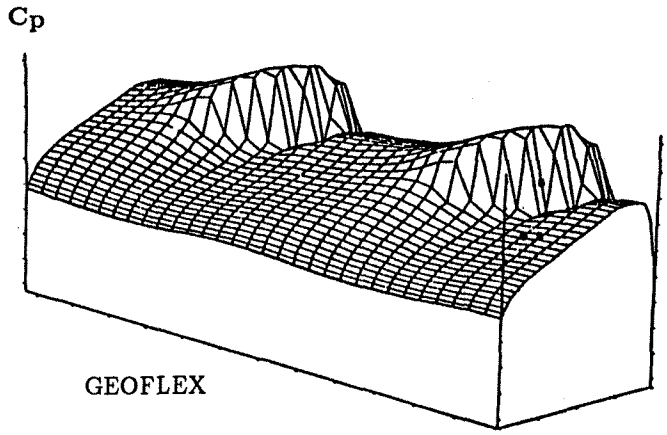

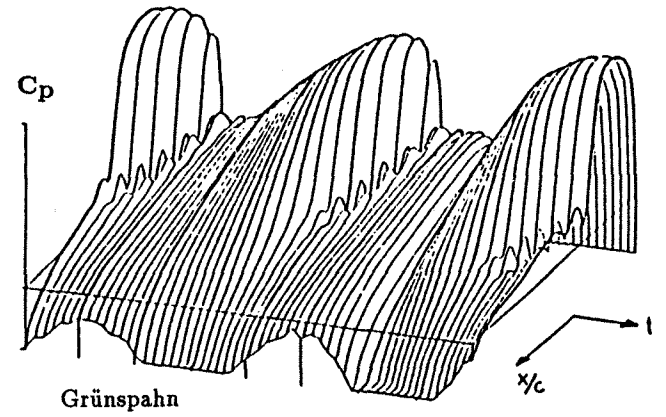

Fig. 12 Pressure distribution for the Grünspahn testcase,
$M_0 = 0.738$, $\Delta M = 0.062$, $\alpha = 0°$, $\omega = 196.4\,[1/s]$.

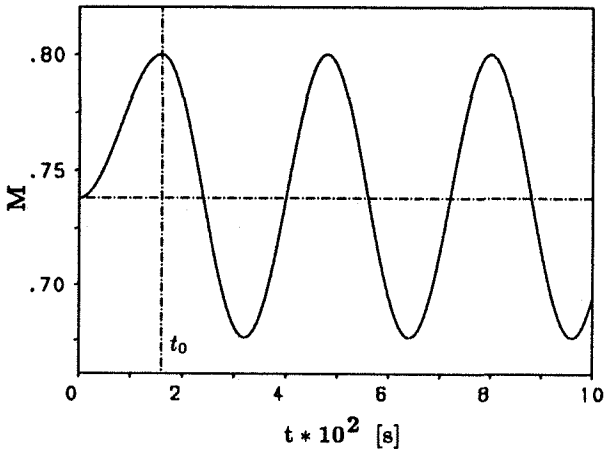

Fig. 13a Mach number function for the Grünspahn testcase.

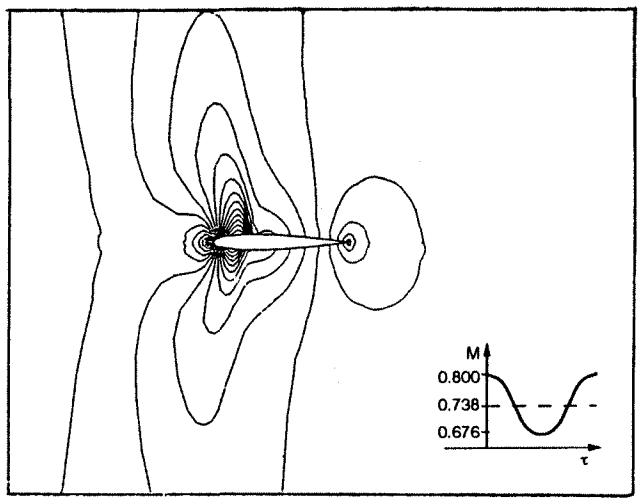

GEOFLEX

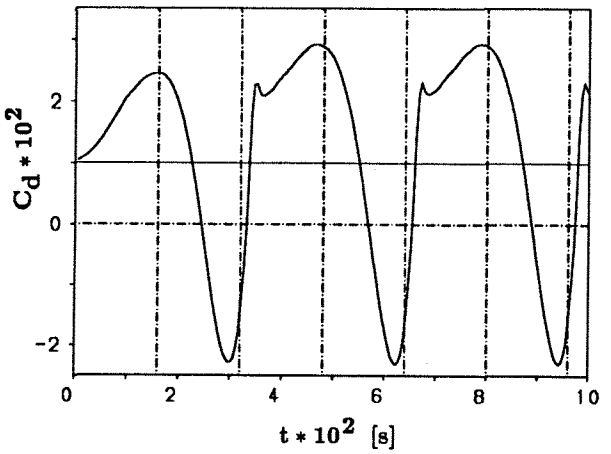

Fig. 13b Drag coefficient for the Grünspahn testcase evaluated with GEOFLEX,
$M_0 = 0.738$, $\Delta M = 0.062$, $\alpha = 0°$, $\omega = 196.4\,[1/s]$.

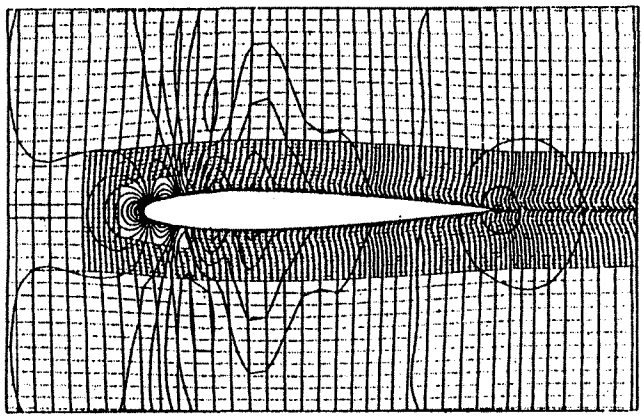

Grünspahn

Fig. 14 Isobares at $t = 0.063\,[s]$ for the Grünspahn testcase,
$M_0 = 0.738$, $\Delta M = 0.062$, $\alpha = 0°$, $\omega = 196.4\,[1/s]$.

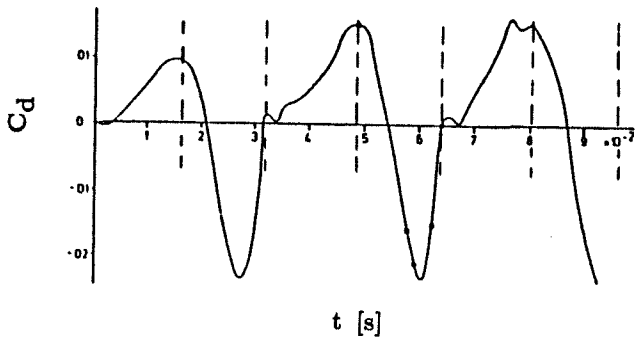

Fig. 13c Drag coefficient for the Grünspahn testcase,[13]
$M_0 = 0.738$, $\Delta M = 0.062$, $\alpha = 0°$, $\omega = 196.4\,[1/s]$.

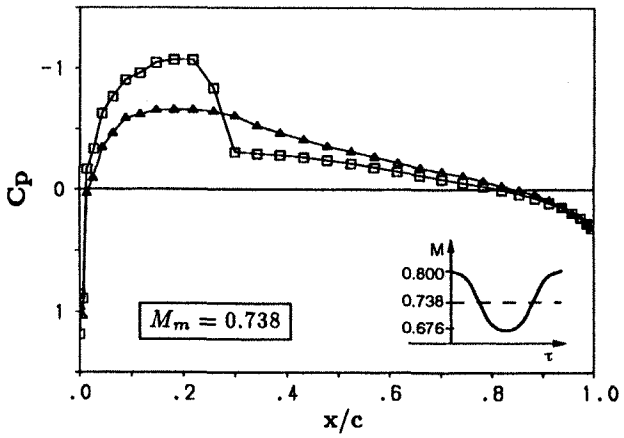

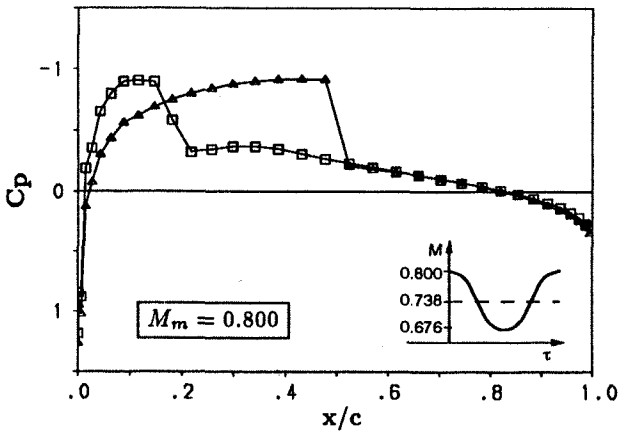

Fig. 15 Pressure distribution for the Grünspahn testcase, $M_0 = 0.738$, $\Delta M = 0.062$, $\alpha = 0°$, $\omega = 196.4\,[1/s]$, □ unsteady, △ steady.

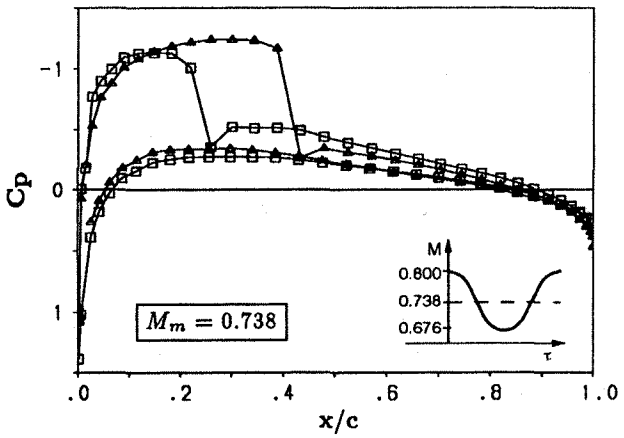

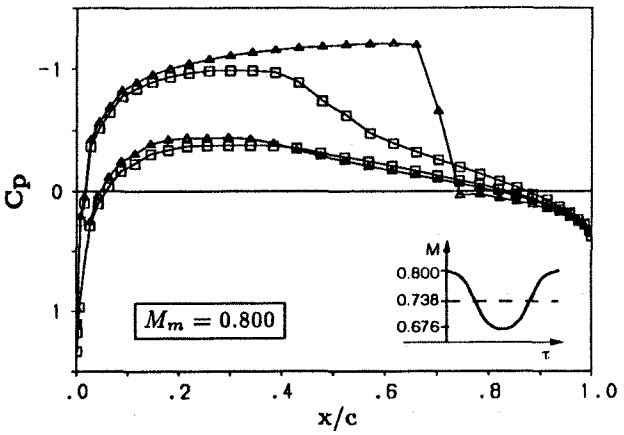

Fig. 16 Pressure distribution for the Grünspahn testcase, $M_0 = 0.738$, $\Delta M = 0.062$, $\alpha = 2°$, $\omega = 196.4\,[1/s]$, □ unsteady, △ steady.

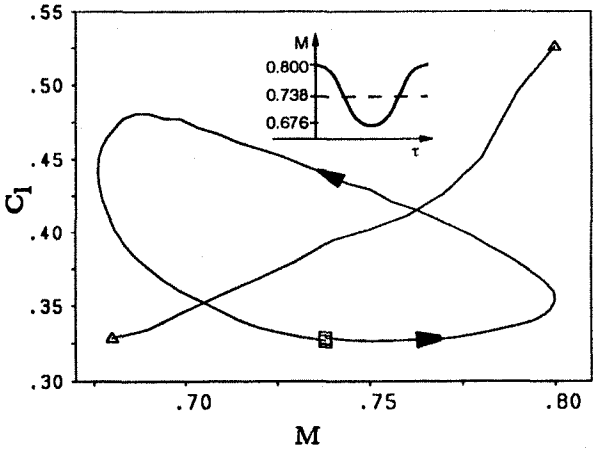

Fig. 17 Lift coefficient for the Grünspahn testcase, $M_0 = 0.738$, $\Delta M = 0.062$, $\alpha = 2°$, $\omega = 196.4\,[1/s]$, □ unsteady, △ steady.

motions of bodies the Euler equations are Galilei–transformed into a body–fixed form. Consequently the used Euler code named GEOFLEX and the farfield boundary conditions have been modified.

Results of Euler codes in inertial formulation addressing a steep Mach number ramp and Mach number oscillations validate GEOFLEX in body–fixed formulation.

Results are shown for two unsteady motions of a NACA 0012 airfoil in transonic and supersonic flow, namely a horizontal acceleration and horizontal oscillations. The acceleration is characterized by an initial, short–time decrease of the lift–coefficient and its following increase to the steady–state value. The corresponding pressure distributions depict the development of the shock clearly. For the case of the horizontal oscillations the inertia of the shock motion results in a time lag of the lift–coefficient and even in negative values of the drag–coefficient caused by shocks moving towards the leading edge. For the supersonic case the influence of the shock is smaller than in the transonic case, because of its position relative to the profile.

References

[1] Laschka, B., Unsteady Flows - Fundamentals and Applications, AGARD CP-386, 1981.

[2] Vicroy, D., Assessment of Microburst Models for Downcraft Estimation, Journal of Aircraft, Vol. 29, No. 6, Nov.–Dec. 1992.

[3] Habibie, I.A., Eulerlösungen für instationär längsbeschleunigte Strömungen um Tragflügelprofile, Ph.D. Thesis, Technische Universität München, 1994.

[4] Hirsch, C., Numerical Computation of Internal and External Flows, Vol. 2, John Wiley & Sons, 1990.

[5] Eberle, A., MBB-EUFLEX. A New Flux Extrapolation Scheme Solving the Euler Equations for Arbitrary 3-D Geometry and Speed, MBB/LKE122/S/PUB/140, 1984.

[6] Weishäupl, C., Analyse verschiedener Wellenmodelle und numerischer Methoden zur verbesserten Stossauflösung in einem Eulerverfahren, Report Nr. 92/36, Lehrstuhl für Fluidmechanik, Technische Universität München, 1992.

[7] Weishäupl, C., Zur physikalischen Stossauflösung in einem Euler-Verfahren, Jahrbuch 1993 der Deutschen Gesellschaft für Luft- und Raumfahrt e.V. (DGLR), Band 1, Bonn, 1993.

[8] Whitfield, D., Janus, J., Three-Dimensional Unsteady Euler Equations Solutions Using Flux Vector Splitting, AIAA-84-1552, 1984.

[9] Hase, R., Einfluss der Fernfeldrandbedingungen auf die numerische Lösung der instationären Eulergleichungen für umströmte Körper, Ph.D. Thesis, Technische Universität München, 1992.

[10] Brenneis, A., Berechnung instationärer zwei- und dreidimensionaler Strömungen um Tragflügel mittels eines impliziten Relaxationsverfahrens zur Lösung der Eulergleichungen, VDI–Verlag, 1989.

[11] Gao, Z., personal communication, 1994.

[12] Rochholz, H., personal communication, 1994.

[13] Grünspahn, K., Numerisches Bicharakteristikenverfahren zur Berechnung stark instationärer Strömungen um Profile, Ph.D. Thesis, Rheinisch-Westfälische Technische Hochschule Aachen, 1988.

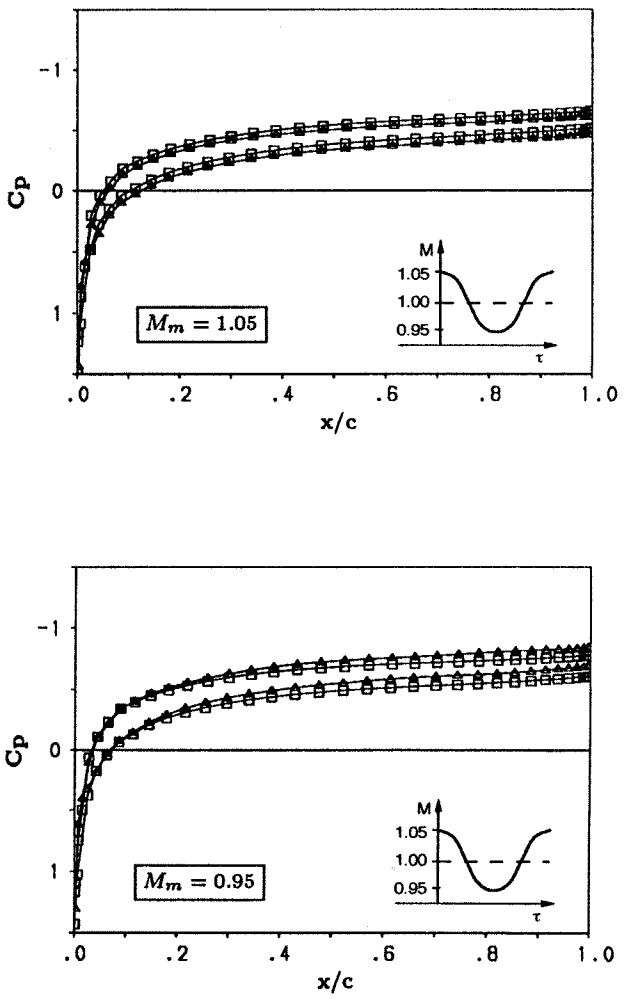

Fig. 18 Pressure distribution for horizontal oscillations in the sonic region,
$M_0 = 1.0$, $\Delta M = 0.05$, $\alpha = 2°$, $k = 0.5$,
□ unsteady, △ steady.

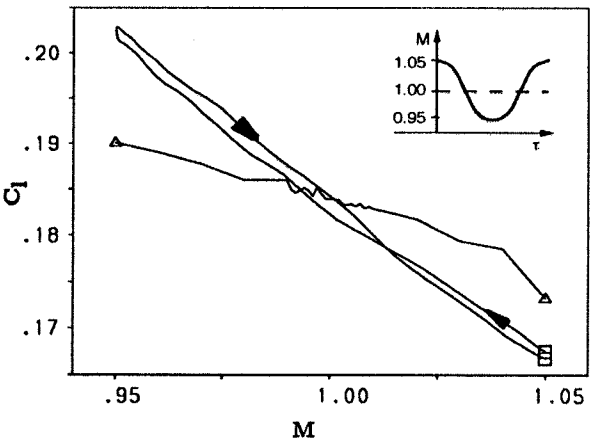

Fig. 19 Lift coefficient for horizontal oscillations in the sonic region,
$M_0 = 1.0$, $\Delta M = 0.05$, $\alpha = 2°$, $k = 0.5$,
□ unsteady, △ steady.

Appendix

$$\underline{R}_k = \begin{pmatrix} \hat{\xi}_{k,x} & \hat{\xi}_{k,y} \\ (u_k - U_0)\,\hat{\xi}_{k,x} & (u_k - U_0)\,\hat{\xi}_{k,y} - \rho_k \hat{\xi}_{k,z} \\ (v_k - V_0)\,\hat{\xi}_{k,x} + \rho_k \hat{\xi}_{k,z} & (v_k - V_0)\,\hat{\xi}_{k,y} \\ (w_k - W_0)\,\hat{\xi}_{k,x} - \rho_k \hat{\xi}_{k,y} & (w_k - W_0)\,\hat{\xi}_{k,y} + \rho_k \hat{\xi}_{k,x} \\ \dfrac{\Phi_k}{\kappa - 1}\hat{\xi}_{k,x} + \rho_k \left((v_k - V_0)\,\hat{\xi}_{k,x} - (w_k - W_0)\,\hat{\xi}_{k,y}\right) & \dfrac{\Phi_k}{\kappa - 1}\hat{\xi}_{k,y} + \rho_k \left((w_k - W_0)\,\hat{\xi}_{k,x} - (u_k - U_0)\,\hat{\xi}_{k,z}\right) \end{pmatrix}$$

$$\begin{pmatrix} \hat{\xi}_{k,x} & \alpha_k & \alpha_k \\ (u_k - U_0)\,\hat{\xi}_{k,x} + \rho_k \hat{\xi}_{k,z} & \alpha_k \left((u_k - U_0) + c\,\hat{\xi}_{k,x}\right) & \alpha_k \left((u_k - U_0) - c\,\hat{\xi}_{k,x}\right) \\ (v_k - V_0)\,\hat{\xi}_{k,x} - \rho_k \hat{\xi}_{k,x} & \alpha_k \left((v_k - V_0) + c\,\hat{\xi}_{k,y}\right) & \alpha_k \left((v_k - V_o) - c\,\hat{\xi}_{k,y}\right) \\ (w_k - W_0)\,\hat{\xi}_{k,x} & \alpha_k \left((w_k - W_0) + c\,\hat{\xi}_{k,z}\right) & \alpha_k \left((w_k - W_0) - c\,\hat{\xi}_{k,z}\right) \\ \dfrac{\Phi_k}{\kappa - 1}\hat{\xi}_{k,x} + \rho_k \left((u_k - U_0)\,\hat{\xi}_{k,y} - (v_k - V_0)\,\hat{\xi}_{k,x}\right) & \alpha_k \left(\dfrac{\Phi + c^2}{\kappa - 1} + c\,\hat{\Theta}_{k,\xi}\right) & \alpha_k \left(\dfrac{\Phi + c^2}{\kappa - 1} - c\,\hat{\Theta}_{k,\xi}\right) \end{pmatrix}$$

with

$$\hat{\xi}_{k,i} = \frac{\xi_{k,i}}{\sqrt{\xi_{k,x}^2 + \xi_{k,y}^2 + \xi_{k,z}^2}} \qquad i = x, y, z$$

$$\hat{\Theta}_{k,\xi} = \hat{\xi}_{k,x}\,(u_k - U_0) + \hat{\xi}_{k,y}\,(v_k - V_0) + \hat{\xi}_{k,z}\,(w_k - W_0)$$

$$\alpha_k = \frac{\rho_k}{\sqrt{2}\,c}$$

$$\Phi_k = \frac{\kappa - 1}{2}\left((u_k - U_0)^2 + (v_k - V_0)^2 + (w_k - W_0)^2\right)$$

$$\underline{L}_k = \underline{R}_k^{-1} = \begin{pmatrix} \hat{\xi}_{k,x}\left(1 - \dfrac{\Phi_k}{c^2}\right) + \dfrac{1}{\rho_k}\left((w_k - W_0)\,\hat{\xi}_{k,y} - (v_k - V_0)\,\hat{\xi}_{k,z}\right) & \hat{\xi}_{k,x}\dfrac{(u_k - U_0)\,(\kappa - 1)}{c^2} \\ \hat{\xi}_{k,y}\left(1 - \dfrac{\Phi_k}{c^2}\right) + \dfrac{1}{\rho_k}\left((u_k - U_0)\,\hat{\xi}_{k,z} - (w_k - W_0)\,\hat{\xi}_{k,x}\right) & -\dfrac{\hat{\xi}_{k,z}}{\rho_k} + \hat{\xi}_{k,y}\dfrac{(u_k - U_0)\,(\kappa - 1)}{c^2} \\ \hat{\xi}_{k,z}\left(1 - \dfrac{\Phi_k}{c^2}\right) + \dfrac{1}{\rho_k}\left((v_k - V_0)\,\hat{\xi}_{k,x} - (u_k - U_0)\,\hat{\xi}_{k,y}\right) & \dfrac{\hat{\xi}_{k,y}}{\rho_k} + \hat{\xi}_{k,z}\dfrac{(u_k - U_0)\,(\kappa - 1)}{c^2} \\ \beta_k\left(\Phi_k - c\,\hat{\Theta}_{k,\xi}\right) & \beta_k\left(c\,\hat{\xi}_{k,x} - (u_k - U_0)\,(\kappa - 1)\right) \\ \beta_k\left(\Phi_k + c\,\hat{\Theta}_{k,\xi}\right) & -\beta_k\left(c\,\hat{\xi}_{k,x} + (u_k - U_0)\,(\kappa - 1)\right) \end{pmatrix}$$

$$\begin{pmatrix} \dfrac{\hat{\xi}_{k,z}}{\rho_k} + \hat{\xi}_{k,x}\dfrac{(v_k - V_0)\,(\kappa - 1)}{c^2} & -\dfrac{\hat{\xi}_{k,y}}{\rho_k} + \hat{\xi}_{k,x}\dfrac{(w_k - W_0)\,(\kappa - 1)}{c^2} & -\hat{\xi}_{k,x}\dfrac{\kappa - 1}{c^2} \\ \hat{\xi}_{k,y}\dfrac{(v_k - V_0)\,(\kappa - 1)}{c^2} & \dfrac{\hat{\xi}_{k,x}}{\rho_k} + \hat{\xi}_{k,y}\dfrac{(w_k - W_0)\,(\kappa - 1)}{c^2} & -\hat{\xi}_{k,y}\dfrac{\kappa - 1}{c^2} \\ -\dfrac{\hat{\xi}_{k,x}}{\rho_k} + \hat{\xi}_{k,z}\dfrac{(v_k - V_0)\,(\kappa - 1)}{c^2} & \hat{\xi}_{k,z}\dfrac{(w_k - W_0)\,(\kappa - 1)}{c^2} & -\hat{\xi}_{k,z}\dfrac{\kappa - 1}{c^2} \\ \beta_k\left(c\,\hat{\xi}_{k,y} - (v_k - V_0)\,(\kappa - 1)\right) & \beta_k\left(c\,\hat{\xi}_{k,z} - (w_k - W_0)\,(\kappa - 1)\right) & \beta_k\,(\kappa - 1) \\ -\beta_k\left(c\,\hat{\xi}_{k,y} + (v_k - V_0)\,(\kappa - 1)\right) & -\beta_k\left(c\,\hat{\xi}_{k,z} + (w_k - W_0)\,(\kappa - 1)\right) & \beta_k\,(\kappa - 1) \end{pmatrix} \qquad \text{with} \quad \beta_k = \frac{1}{\sqrt{2}\rho c}$$